Tellus SERIES A DYNAMIC METEOROLOGY AND OCEANOGRAPHY
PUBLISHED BY THE INTERNATIONAL METEOROLOGICAL INSTITUTE IN STOCKHOLM

The Arctic and Polar cells act on the Arctic sea ice variation

By WEIHONG QIAN[1]*, KAIJUN WU[1] and DELIANG CHEN[2], [1]*Department of Atmospheric and Oceanic Sciences, School of Physics, Peking University, Beijing 100871, China*; [2]*Department of Earth Sciences, University of Gothenburg, Gothenburg, Sweden*

(Manuscript received 23 February 2015; in final form 1 July 2015)

ABSTRACT

The Arctic sea ice has undergone a substantial long-term decline with superimposed interannual sea ice minimum (SIM) events over the last decades. This study focuses on the relationship between atmospheric circulation and the SIM events in the Arctic region. Four reanalysis products and simulations of one climate model are first analysed to confirm the existence of the Arctic cell, a meridional circulation cell to the north of 80°N, by visualising through the mean streamline and mean mass stream function in the Northern Hemisphere. Dynamical analyses of zonally averaged stationary eddy heat and momentum fluxes as well as the global precipitation rate data further confirm its existence. Finally, we found that the change in the Arctic sea ice concentration lags the variations of the descending air flow intensity associated with the Polar and Arctic cells, by about 2 months for the climatic annual cycle and about 10 months for the interannual anomaly. Five Arctic SIM events during the last three decades support this relationship. These results have implications for understanding the relationship between atmospheric circulation and sea-ice variations, and for predicting the Arctic sea ice changes.

Keywords: Arctic, Polar cell, Arctic cell, sea ice minimum, stream function

1. Introduction

The traditional three-cell model was firstly proposed by Ferrel in 1860 (Persson, 2006) and has been widely accepted in the past century. The model describes that the Hadley cell ranges from the equator to about latitudes of 30°N, the Polar cell covers from about 60°N to the poles, and the Ferrel cell exists between them in the Northern Hemisphere (NH). Ferrel believed that the three meridional cells are equally crossing about 30 latitudes in each hemisphere. However, the Polar cell, in theory, cannot cross as many latitudes as the Hadley cell does in the lower latitudes because a larger decrease in the rotational radius will cause a larger increase in westerly velocity aloft according to the conservation of angular momentum (Ahrens, 2012).

Recently, Qian et al. (2015a) proposed a fourth meridional cell, named the Arctic cell, based on the analyses of meridional–vertical section streamline (MSS) and meridional-mass stream function (MSF). The Arctic cell was found existing in the troposphere to the north of 80°N, and its intensity is too weak to be compared with other three cells. Due to the sparse long-term atmospheric radiosonde observations in the Arctic troposphere (Kahl et al., 1992), researches on the Arctic cell depend upon the observational datasets and climate model simulations as well as visualisation methods. Therefore, more analyses on different datasets and simulations are required to prove the existence of the Arctic cell.

The meridional circulation variation is considered to play an important part in climate change, such as the intensity and coverage of the Hadley cell (Hu and Fu, 2007; Chen et al., 2014b) cannot directly explain the fast climate warming and interannual sea ice minimum (SIM) events in the Arctic (Kumar et al., 2010; Graversen et al., 2011; Devasthale et al., 2013; Dong et al., 2014). In the Arctic, one of the most concerned topics is the interaction between sea ice and atmospheric circulation. Arctic sea ice has undergone a substantial long-term decline (Serreze et al., 2007; Graversen et al., 2008; Screen and Simmonds, 2010; Ding et al., 2014) with superimposed interannual SIM events (Kay et al., 2008; Graversen et al., 2011; Bennartz et al., 2013; Parkinson and Comiso, 2013) over the last decades. Various feedback processes were considered to

*Corresponding author.
email: qianwh@pku.edu.cn

Tellus A 2015. © 2015 W. Qian et al. This is an Open Access article distributed under the terms of the Creative Commons Attribution 4.0 International License (http://creativecommons.org/licenses/by/4.0/), allowing third parties to copy and redistribute the material in any medium or format and to remix, transform, and build upon the material for any purpose, even commercially, provided the original work is properly cited and states its license.

Citation: Tellus A 2015, **67**, 27692, http://dx.doi.org/10.3402/tellusa.v67.27692

exist in the Arctic atmosphere-ocean-ice interaction (Hansen and Nazarenko, 2004; Shindell and Faluvegi, 2009; Vihma, 2014) including the role played by meridional heat transport via the atmosphere (Jeong et al., 2014), but there is no consensus on the relative importance of various factors responsible for the Arctic amplification and sea ice decline.

Beside feedback mechanisms, storm tracks, jet stream and planetary waves also played important roles in the Arctic sea ice change (Cohen et al., 2014). Honda et al. (2009) and Sato et al. (2014) showed that late autumn-early winter atmospheric anomalies can force an immediate, local and direct atmospheric response to the warm anomalies locally over the Barents and Kara seas, which in turn change the baroclinicity and affects large-scale planetary or Rossby waves in the atmosphere. Jaiser et al. (2012) found that early autumn sea ice anomalies can force a delayed, remote and indirect atmospheric response through altered baroclinicity and synoptic–planetary wave interaction, or through increased Eurasian snow cover and high pressure over the Barents and Kara seas that force upward propagating planetary waves into the stratosphere. The 'summertime' Arctic sea ice concentration's influence on the following 'wintertime' climate and circulation variability suggested a potential application in operational seasonal climate and circulation forecasts, although it is unclear whether late summer and early autumn, or late autumn and early winter sea-ice anomalies are more skilful at predicting the winter weather patterns. As summarised by Cohen et al. (2014) as well as Deser and Teng (2008a), observational analyses have shown significant correlation between reduced Arctic sea-ice cover and the negative phase of the winter North Atlantic Oscillation/Arctic Oscillation (NAO/AO) and Northern Annular Mode (NAM). On the other hand, numerous studies indicate that the atmospheric circulation played an important role in driving Arctic sea ice declines (Rigor et al., 2002; Hu et al., 2002; Serreze and Francis, 2006; Ukita et al., 2007; Deser and Teng, 2008b; Jeong et al., 2014), particularly showing that summer sea ice variations appear to be initiated by atmospheric circulation anomalies over the high Arctic in late spring (Deser et al., 2000). The consensus of the observational studies suggested that interannual variability in sea ice conditions is caused by the variability in the large scale atmospheric circulation, which locally manifests itself as surface air temperature and wind anomalies (Prinsenberg et al., 1997).

In order to confirm the existence of the Arctic cell and its effect on the Arctic sea ice variation, this paper first analyses four reanalysis products, one climate model simulation and one precipitation rate data by both qualitative and quantitative methods. Then we explore the possible relationship between the Arctic sea ice change and meridional circulation in the NH high latitudes. After this introduction, Section 2 describes the datasets and methodology used in this study. The existence of the Arctic cell is quantitatively confirmed in Section 3 and dynamically explained in Section 4, respectively. A phase-difference relationship between the SIM events and descending flow intensity (DFI) anomalies associated with the Polar and Arctic cells in the NH is illustrated in Section 5. Finally, conclusions are given in Section 6.

2. Datasets and methodologies

2.1. Datasets

Studies of zonally averaged meridional mean circulation require global observations (e.g. satellites or other large-scale upper-air observations), reanalysis datasets and atmospheric general circulation models (GCMs) to give a comprehensive description of the phenomenon. Four daily-mean reanalysis products, and one ensemble mean Community Earth System Model version 1 (CESM1) (CAM5) model simulation with three historical runs as well as a global precipitation rate and sea ice concentration (SIC) dataset are used in this paper. The first two reanalysis products are two NCEP Reanalyses (R1 and R2) from 1979 to present (Kalnay et al., 1996; Kanamitsu et al., 2002) with a horizontal 2.5-degree longitude–latitude resolution and 17 vertical levels, retrieved from the websites (www.esrl.noaa.gov/psd/data/gridded/data.ncep.reanalysis.html; www.esrl.noaa.gov/psd/data/gridded/data.ncep.reanalysis2.html). The third reanalysis product is the ERA Interim Reanalysis dataset from 1979 to present (Dee et al., 2011) with a horizontal 0.75-degree longitude–latitude resolution and 37 vertical levels, retrieved from the website (www.ecmwf.int/research/era/do/get/index). The fourth is the Japanese 55-yr Reanalysis (JRA-55) product from 1958 to present (Onogi et al., 2007; Ebita et al., 2011; Chen et al., 2014a) provided by the Japan Meteorological Agency with a horizontal 1.25-degree longitude–latitude resolution and 37 vertical levels, retrieved from the website (www.rda.ucar.edu/datasets/ds628.1/).

Differences among reanalysis products depend on the quantity and quality of original observations and assimilation methods used. Each reanalysis product was developed to meet specific goals with different physical parametric processes and resolutions. Nearly all of the existing reanalysis products ingest a variety of surface, upper-air and satellite observations (when available) using either a three-dimensional variational (3D-VAR) or four-dimensional variational (4D-VAR) assimilation technique. The NCEP R1 and R2 datasets belong to the older 3D-VAR assimilation reanalysis products. To avoid the errors caused by sparse data coverage in some regions, particularly in the Antarctic and Arctic regions, the ERA Interim and the JRA-55 datasets, which are 4D-VAR assimilation reanalysis products,

are also used. In the Arctic, the skills of these reanalysis products have improved due to the assimilated satellite and radiosonde datasets since 1979 (Bromwich et al., 2007). To ensure comparability, this paper uses the four reanalysis products for the same period of 1979–2013.

Beyond 80°N, the historical radiosonde observations are sparse with about five stations from the beginning of record through 1987 (Kahl et al., 1991, 1992). Due to the weakness of the reanalysis products over the Arctic Ocean associated with the absence of long-term atmospheric radiosonde observations for data assimilation, simulation from one of CMIP5 (phase 5 of the Coupled Model Intercomparison Project) (Taylor et al., 2012) climate models is also used in this study to confirm the existence of the Arctic cell. The model results used are from a set of experiments of the CESM1 that includes the Community Atmospheric Model version 5 (CAM5) referred to herein as CESM1 (CAM5) (Neale et al., 2010). The ensemble mean CAM5 model dataset with three historical runs from 1850 to 2005 has a horizontal 0.9375×1.25-degree latitude–longitude resolution and 17 vertical levels, retrieved from the website (www.earthsystemgrid.org/home.htm). Within a given model's ensemble of historical runs, three members in the pre-industrial control run are forced in the same way, but each is initiated from a slightly different point. Different initial conditions produce different climate trajectories, with each realisation assumed to be an equally likely outcome (Taylor et al., 2012). The model simulation is used as an independent data to compare with the result of the four reanalysis products.

The Climate Prediction Center (CPC) Merged Analysis of Precipitation (CMAP) is used to examine the climatic precipitation rate near the Arctic and in the sub-polar zone associated with different vertical circulations. The CMAP dataset consists of pentad-mean precipitation rate from 0 to 73 pentads per year, with the 12th pentad covering Feb 25–Mar 1 whether or not there is a leap year (Xie and Arkin, 1997). The standard version of CMAP is obtained from five kinds of satellite estimates (GPI, OPI, SSM/I scattering, SSM/I emission and MSU), while the enhanced version also includes blended NCEP/NCAR Reanalysis Precipitation values. The spatial resolution of the CMAP dataset is 2.5-degree latitude–longitude interval and the temporal coverage is from 1979 to present. The data were retrieved from the website: www.esrl.noaa.gov/psd/data/gridded/data.cmap.html#detail.

The monthly-mean gridded SIC and sea ice extent (SIE) from the HadISST1 version for 1979–2013 (Rayner et al., 2003) are used to characterise sea-ice variations. HadISST1 replaces the global sea ice and sea surface temperature (SST) datasets and is a unique combination of monthly-mean global fields of SST and SIC on a 1-degree latitude–longitude grid from 1871 to present. It was retrieved from the website: www.metoffice.gov.uk/hadobs/hadisst/. The sea ice fields are made more homogeneous by compensating satellite microwave-based SICs for the impact of surface melt effects on retrievals in the Arctic and for algorithm deficiencies in the Antarctic, and by making the historical in situ concentrations consistent with the satellite data.

2.2. Methodology

The monthly-mean and seasonal-mean climatology of variables are used in this study. A monthly-mean atmospheric variable field $F_{m,y}$ (λ, φ, p, t) can be decomposed into its climatology $\tilde{F}_m(\lambda, \varphi, p)$ and temporal deviation $F'_{m,y}(\lambda, \varphi, p, t)$ on a calendar month t in year y at a spatial point of pressure level p, longitude λ and latitude φ, i.e.

$$F_{m,y}(\lambda, \varphi, p, t) = \tilde{F}_m(\lambda, \varphi, p) + F'_{m,y}(\lambda, \varphi, p, t) \qquad (1)$$

In eq. (1), the subscript m indicates monthly mean, which in this case is the 30-yr (1981–2010) average of an observed or reanalysis variable field on the calendar month m. For example, when m is set to May, t is the months from May 1981, May 1982, …, May 2010 for total 30 yr.

$$\tilde{F}_m(\lambda, \varphi, p) = \sum_{y=1981}^{2010} F_{t=m,y}(\lambda, \varphi, p, t)/30 \qquad (2)$$

The climatic mean field or climatology defined in eq. (2) varies from month to month, depicting a seasonal cycle. Climatic seasonal-mean field $\tilde{F}_s(\lambda, \varphi, p)$ and climatic annual-mean field $\tilde{F}_a(\lambda, \varphi, p)$ can be calculated by monthly-mean fields.

Using eq. (1), the global tropospheric monthly-mean geopotential height, temperature and wind anomalies can be extracted. In recent years, daily anomalies of atmospheric variables have been used in short-, medium- and extended-range forecasts of many surface weather extremes in China, including heat waves (Ding and Qian, 2012), unusual typhoon tracks (Qian et al., 2014; Huang et al., 2015), summer cold spells in Northeast China (Qian and Jiang, 2014), as well as spring and autumn anomalous low temperature spells in southern China (Qian et al., 2015b). A strategy is to find a connection between these weather extremes and atmospheric variable anomalies. Applying the decomposition approach on the above seven datasets, we examine the relation between Arctic SIM events and atmospheric variable anomalies.

In this paper, monthly-mean wind vector $\vec{V}_m(\lambda, \varphi, p, t) = \vec{i}u_m(\lambda, \varphi, p, t) + \vec{j}v_m(\lambda, \varphi, p, t) + \vec{k}\omega_m(\lambda, \varphi, p, t)$ consists of three components: zonal wind velocity u, meridional wind velocity v and vertical pressure velocity ω (positive downward) or z component velocity $\vec{k}w_m(\lambda, \varphi, p, t)$ (positive upward). A zonally averaged monthly-mean climatic

wind vector $\vec{V}_m(\varphi,p)$ at a specific month of a year t is calculated by

$$\left[\tilde{\vec{V}}_m(\varphi,p)\right]=\sum_{t=1}^{N}\sum_{\lambda=1}^{K}\vec{V}_m(\lambda,\varphi,p,t)/(K\times N), \quad (3)$$

where $N=30$ yr from 1981 to 2010, K is the total grid number along a zonal circle, and m represents the month. Similarly, the zonally averaged seasonal-mean and annual-mean climatic wind vectors can also be calculated from the monthly-mean climatic wind vector. The zonally averaged deviation of climatic monthly-mean wind vector is

$$\tilde{\vec{V}}^{*}_m(\lambda,\varphi,p)=\tilde{\vec{V}}_m(\lambda,\varphi,p)-\left[\tilde{\vec{V}}_m(\varphi,p)\right], \quad (4)$$

of which the two components, $\tilde{u}^{*}_m$ and $\tilde{v}^{*}_m$, can produce the stationary meridional eddy transport $[\tilde{v}^{*}_m\tilde{u}^{*}_m]$.

Meridional cells can be visualised by wind vectors, but the zonally averaged monthly-mean vertical pressure velocity is too small when compared with the zonally averaged monthly-mean horizontal velocity. Therefore, to clearly show the meridional cells, the MSS is first used to depict their spatial structure. The streamline is simply drawn using the grid meridional velocity and vertical pressure velocity magnified by 1000 times so that there is no boundary effect near the North Pole. However, the MSS structure cannot quantitatively illustrate the intensity of each cell. Usually, zonally averaged meridional cells are considered as non-divergent flow so it can be examined using the MSF, which has been used in many previous studies (Lindzen and Hou, 1988; Mitas and Clement, 2005; Hu and Fu, 2007; Chen et al., 2014b), to estimate the intensity evolution of Hadley cell. Note that most MSF analyses were limited to 60°N, and a few to 80°N, in the previous studies.

The meridional stream function, $\psi(\varphi, p)$, satisfying the zonally averaged continuity equation in spherical coordinates, can be calculated at each pressure level, p, and latitude, φ, using the meridional wind integrated (Stachnik and Schumacher, 2011). To reduce the impact of deviation induced by terrains on MSF calculation, we calculated $\psi_1(\lambda, \varphi, p)$ with meridional wind integrated from the bottom (surface pressure p_s) to the top (100 hPa) and $\psi_2(\lambda, \varphi, p)$ from the top to the bottom, respectively, at every grid with boundary conditions as $\psi(\lambda,\varphi,p_{top})=\psi(\lambda,\varphi,p_s)=\psi(\lambda,\varphi_{p_S},p)=\psi(\lambda,\varphi_{p_N},p)=0$. The φ_{p_N} is the North Pole while the φ_{p_S} is the South Pole. Then we use an improved approach proposed by Wang (1994) and Gon et al. (2002), who used two linear weighting functions $W_1(\lambda,\varphi,p)=p/p_s$ and $W_2(\lambda,\varphi,p)=1-p/p_s$ to calculate the weighted MSF as

$$\psi(\lambda,\varphi,p)=W_1(\lambda,\varphi,p)\psi_1(\lambda,\varphi,p)+W_2(\lambda,\varphi,p)\psi_2(\lambda,\varphi,p) \quad (5)$$

at every grid. Finally, the zonal mean $\psi(\varphi, p)$ is obtained.

It is well-known that the Hadley cell is thermally driven and its boundary is set by the conservation of angular momentum, while the Ferrel cell is eddy driven (Holton, 2004). The zonally averaged momentum and thermodynamic energy equations for quasi-geostrophic motions on the middle latitude β plane can be written as:

$$\frac{\partial[\tilde{u}]}{\partial t}-f_0[\tilde{v}]=-\frac{\partial[\tilde{u}^{*}\tilde{v}^{*}]}{\partial y}+[\tilde{X}], \quad (6)$$

$$\frac{\partial[\tilde{T}]}{\partial t}+N^2HR^{-1}[\tilde{w}]=-\frac{\partial[\tilde{v}^{*}\tilde{T}^{*}]}{\partial y}+\frac{[\tilde{J}]}{c_p}, \quad (7)$$

where $[\tilde{u}]$, $[\tilde{v}]$, and $[\tilde{w}]$ are the zonally averaged climatic westerly, southerly and z vertical components of velocity, $[\tilde{T}]$ is the zonally averaged climatic temperature, $\left[\tilde{v}^{*}\tilde{T}^{*}\right]$ and $[\tilde{v}^{*}\tilde{u}^{*}]$ are the zonally averaged stationary eddy heat and eddy momentum fluxes, $[\tilde{X}]$ and $[\tilde{J}]$ are the zonally averaged climatic turbulent drag and diabatic heating rate, N is the buoyancy frequency defined by $N^2\equiv\frac{R}{H}\left(\frac{\kappa T_0}{H}+\frac{dT_0}{dz}\right)$, in which H is scale height, R is the gas constant for dry air and c_p is the specific heat of dry air constant pressure.

If $[\tilde{u}]$ and $[\tilde{T}]$ are steady, namely $\frac{\partial[\tilde{u}]}{\partial t}=\frac{\partial[\tilde{T}]}{\partial t}=0$, the zonally averaged climatic direct circulation ($[\tilde{v}]_d$ and $[\tilde{w}]_d$) is mainly forced by the zonally averaged climatic turbulent drag and diabatic heating rate

$$-f_0[\tilde{v}]_d=[\tilde{X}], \quad (8.1)$$

$$N^2HR^{-1}[\tilde{w}]_d=\frac{[\tilde{J}]}{c_p}, \quad (8.2)$$

while the indirect circulation ($[\tilde{v}]_i$ and $[\tilde{w}]_i$) is mainly driven by the zonally averaged stationary eddy heat and momentum fluxes

$$N^2HR^{-1}[\tilde{w}]_i=-\frac{\partial[\tilde{v}^{*}\tilde{T}^{*}]}{\partial y}, \quad (9.1)$$

$$-f_0[\tilde{v}]_i=-\frac{\partial[\tilde{u}^{*}\tilde{v}^{*}]}{\partial y}. \quad (9.2)$$

The two terms, $\left[\tilde{v}^{*}\tilde{T}^{*}\right]$ and $[\tilde{u}^{*}\tilde{v}^{*}]$, can be calculated using reanalysis products while other two terms $[\tilde{X}]$ and $[\tilde{J}]$ are difficult to obtain directly. The four terms together contribute to form the total circulation.

3. Structure of the Arctic cell

Monthly-mean atmospheric variables and anomalies are often used in climatological research. Figure 1 shows zonally averaged meridional cells depicted by vertical sections of streamline and westerly/easterly velocities calculated in an individual month of September 2005 using the monthly-mean NCEP R1, NCEP R2, ERA Interim,

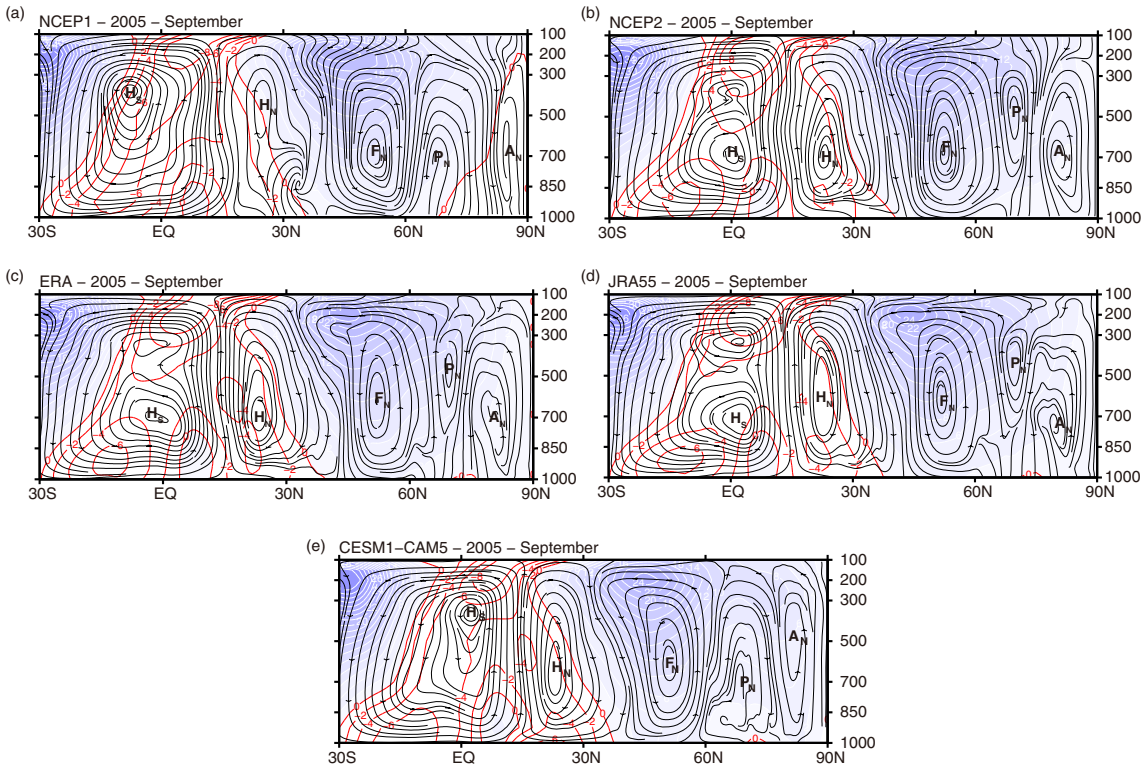

Fig. 1. Five zonally averaged meridional cells described by the vertical–latitude sections of streamline and westerly (shading, 2 m s^{-1} interval) or easterly (red line, 2 m s^{-1} interval) velocities calculated in September 2005 using the monthly-mean (a) NCEP R1, (b) NCEP R2, (c) ERA Interim, (d) JRA-55 and (e) CESM1-CAM5. Symbols of H_N, F_N, P_N and A_N indicate the Hadley, Ferrel, Polar and Arctic cells in the Northern Hemisphere, while H_S indicates the Hadley cell in the Southern Hemisphere.

and JRA-55 reanalysis products, as well as the CESM1-CAM5 model simulation. The meridional streamline is simply drawn using the monthly-mean wind components v_m (φ, p, t) and ω_m (φ, p, t) in September 2005. Five centres of meridional cells covering between 30°S and 90°N are clearly observed in each of the datasets in Fig. 1. The two Hadley cells are well defined from around 30°S to 30°N with an ascending flow in the tropic and two descending flows in the two subtropical zones. The northeasterly trade wind zone in the NH and the southeasterly trade wind zone in the Southern Hemisphere (SH) are commonly observed in the tropical lower troposphere and asymmetrically relative to the equator from five datasets. The flow in the NH is characterised by westerly jet with the maximum zonal velocity (a core) at about 40°N near the tropopause in September. In the SH, two cores of the subtropical jet stream (30°S) and the polar jet stream (50°S) can be calculated from pentad-mean westerly velocity, particularly in the austral winter at the upper troposphere (Qian et al., 2015a). However, only one core (40°N) extends its maximum westerly velocity northward to the polar zone (60–70°N) in the NH, since synoptic-scale eddies are more obvious and active in the NH high latitudes so polar jet stream centres are spatially located in several geographical places separately.

Beyond 40°N, there are three meridional cells. If we draw the meridional cells in April, the two Hadley cells are almost symmetrical relative to the equator. In that case, the Ferrel cell ranges from 30° to 60° latitudes and appears as a reversed and closed loop next to the Hadley cell. Conventionally, the Polar cell is modelled between 60° latitude and the pole (Persson, 2006). However, the meridional streamline of the Polar cell shown in Fig. 1 is bounded between 60 and 80°N in all five datasets. The fourth cell, named as the Arctic cell by Qian et al. (2015a), is clearly observed with its centre located between 80°N and the North Pole. The descending flow branch appears between the two centres of the Polar and Arctic cells. Beyond the centre of Arctic cell there is a branch of ascending flow near the North Pole. This study shows that the four cells in the NH can be found in most of monthly-mean streamlines of four reanalysis products and the model simulation.

To examine the seasonal features, Fig. 2 shows vertical sections of climatic seasonal-mean streamline and westerly (or easterly) wind velocities averaged over 30 yr (1981–2010) using the ERA-Interim reanalysis in the four boreal

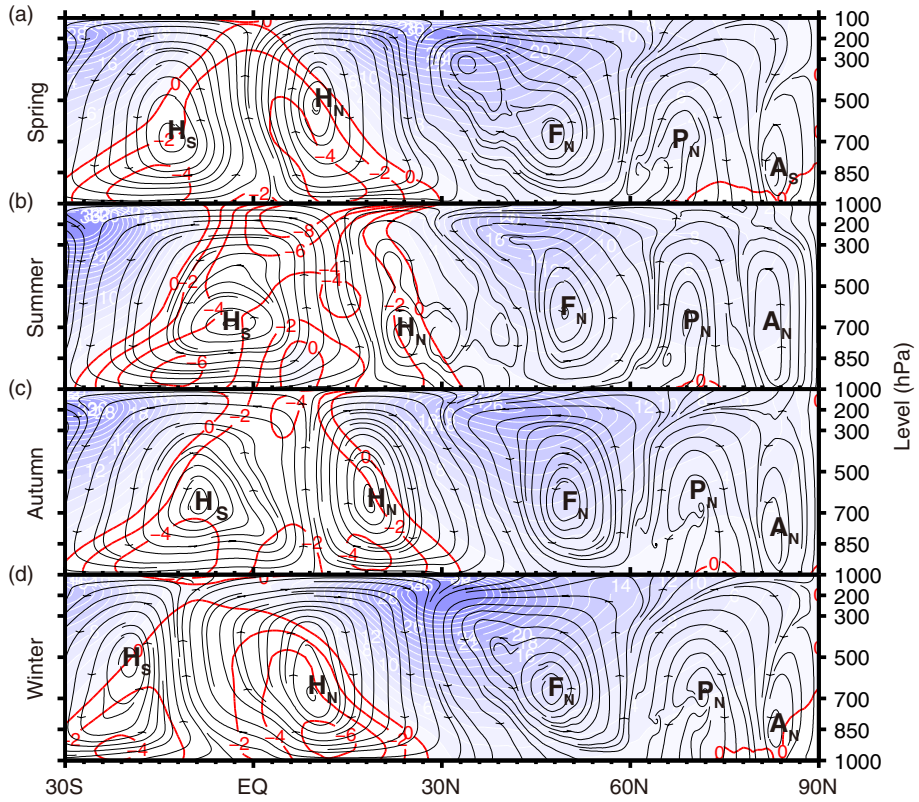

Fig. 2. Five zonally averaged meridional cells described by the vertical-latitude sections of climatic seasonal-mean streamline and westerly (shading, 2 m s^{-1} interval) or easterly (red line, 2 m s^{-1} interval) wind velocities averaged over 30 yr (1981–2010) using the ERA-Interim reanalysis product in the boreal (a) spring, (b) summer, (c) autumn and (d) winter.

seasons. It is noted that the central locations of the four cells vary with different seasons. The centres of two Hadley cells have the largest seasonally migration. In the boreal spring, the Ferrel cell even splits into two centres in the NH, probably because the Ferrel cell is an indirect circulation caused mainly by eddies. The Polar and Arctic cells are always limited in the high latitudes between 60 and 90°N. The easterly flow is stably observed in the tropical troposphere associated with the Hadley cell, but the westerly flow in the polar region is highly unstable since there are strong interactions between the meridional cells and the synoptic eddies as well as the influences from the topographic, frictional and diabatic processes. The same result can also be illustrated from other reanalysis products and model simulations including MERRA (Rienecker et al., 2011), 20CR (Compo et al., 2011) or CFSR (Saha et al., 2010) as well as other climatic model simulations from CMIP5 (Taylor et al., 2012) (not shown).

As we mentioned, while the MSS clearly depicts the spatial structures and basic patterns of the four cells in the NH, the MSF can quantitatively illustrate the intensity of each cell. Five zonally averaged meridional cells illustrated by the vertical section of climatic seasonal-mean MSFs averaged over 30 yr (1981–2010) are shown in Fig. 3 by using the ERA Interim reanalysis in the four boreal seasons. The central intensities and locations of two Hadley cells, as expected, vary with seasons. The Hadley cell in the NH has the minimal (maximal) MSF value 25×10^6 ton s^{-1} (200×10^6 ton s^{-1}) and the northernmost (southernmost) latitude in the boreal summer (winter). The central MSF value gradually reduces from the Ferrel cell to the Polar and Arctic cells so the MSF interval is drawn as 25×10^6 ton s^{-1} between 30°S and 30°N, 5×10^6 ton s^{-1} between 30°N and 62.25°N and 1×10^6 ton s^{-1} between 62.25 and 90°N in Fig. 3. It is noted that the Arctic cell is influenced by the Polar cell in terms of intensities and locations. As illustrated in Figs. 2 and 3, the central location of the Arctic cell is generally lower than that of the Polar cell. In the boreal winter, however, the central location of the Arctic cell is entirely located beneath the Polar cell, when the intensity of the Polar cell reaches its maximum (Fig. 3d). In contrast, the Arctic cell stands alongside the Polar cell in summer when the Polar cell is relatively weak (Fig. 3b). The similar distributions of MSFs can also be observed from other reanalysis products and model simulations.

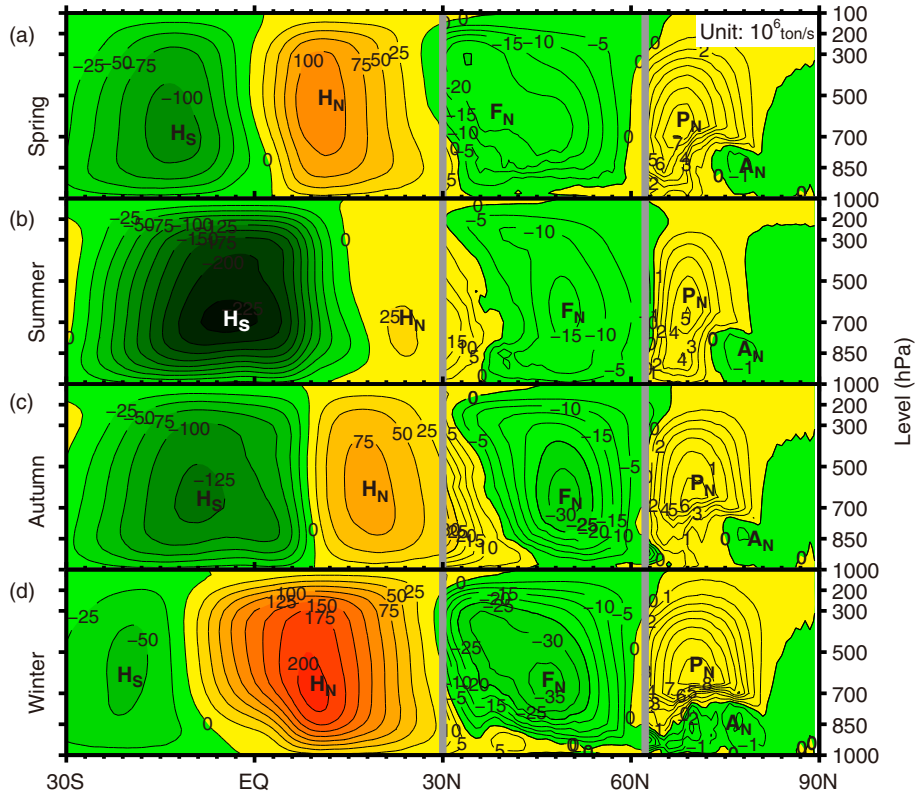

Fig. 3. Five zonally averaged meridional cells described by the vertical-latitude section of climatic seasonal-mean MSFs (yellow-red shading for positive and green shading for negative) averaged over 30 yr (1981–2010) by the ERA Interim reanalysis product in the boreal (a) spring, (b) summer, (c) autumn and (d) winter. The MSF interval is 25×10^6 ton s^{-1} between 30°S and 30°N, 5×10^6 ton s^{-1} between 30 and 62.25°N and 1×10^6 ton s^{-1} between 62.25 and 90°N. Symbols of H_N, F_N, P_N and A_N indicate the Hadley, Ferrel, Polar and Arctic cells in the Northern Hemisphere, while H_S indicates the Hadley cell in the Southern Hemisphere.

Two pairs of meridional cells in the NH are well defined using the two 4D-VAR ERA and JAR-55 reanalysis products in Fig. 4. The first pair is the Hadley and Ferrel cells, whose monthly-mean intensities are in climatic annual cycle and opposite in phase (Fig. 4a). The MSF difference between the Hadley and Ferrel cells is maximum in January and minimum in July. Similarly, the intensity difference between the second pair (the Polar and Arctic cells) is also maximum in January and minimum in July (Fig. 4b).

The climatic annual-mean MSF averaged over 30 yr (1981–2010) of the four reanalysis products of NCEP R1, NCEP R2, ERA Interim, JRA55, and the ensemble mean data of three CAM5 historical runs are displayed in Fig. 5. All four cells are commonly observed in the NH with comparable central intensities and locations. As an independent dataset of model simulation, CESM1 (CAM5) also shows the same structure of four cells observed in the four reanalysis products in the NH. The intensity ratio of the Ferrel, Polar and Arctic cells to the Hadley cell are about 1:3, 1:13 and 1:80, respectively, while the intensity ratio of the Arctic cell to the Polar cell is 1:6. Although the intensity of the Arctic cell is very weak, its existence shows an opposite circulation pattern in the NH high latitudes. The descending flow is seasonally located between the Polar and Arctic cells in the boundary of positive and negative MSFs while the ascending flow is in the north side of the Arctic cell centre.

Figure 6 shows the consistent interannual intensity variability of the Polar and Arctic cells based on the four reanalysis products. At the same time, it also shows that several large fluctuations were not reproduced by the ensemble mean simulation of the model historical runs. Further, there appears to be a relationship between the intensities of the Polar and Arctic cells.

4. Existence of the Arctic cell

Using four reanalysis products and one model simulation, we have revealed that there are four meridional cells in the NH from individual monthly-mean and climatic seasonal-mean streamlines as well as climatic seasonal-mean and annual-mean MSFs. The dynamical explanations

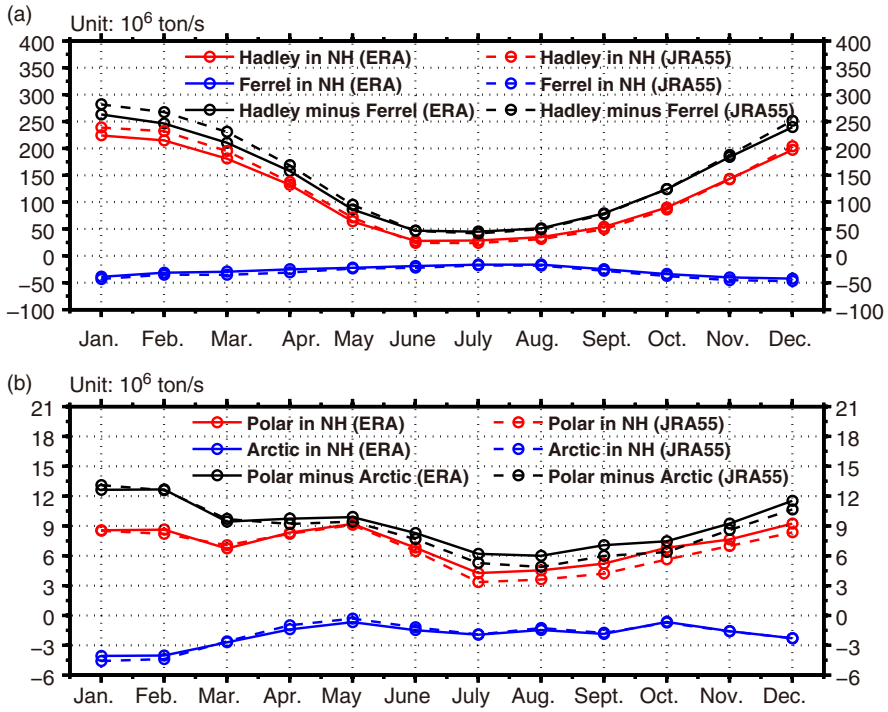

Fig. 4. Monthly-mean intensities of the four cells in the Northern Hemisphere. The MSF intensities (red and blue lines, 10^6 ton s^{-1}) of (a) the Hadley and Ferrel cells and their differences (black line, 10^6 ton s^{-1}) based on ERA and JRA55 reanalysis products; (b) same as (a) but for the Polar and Arctic cells.

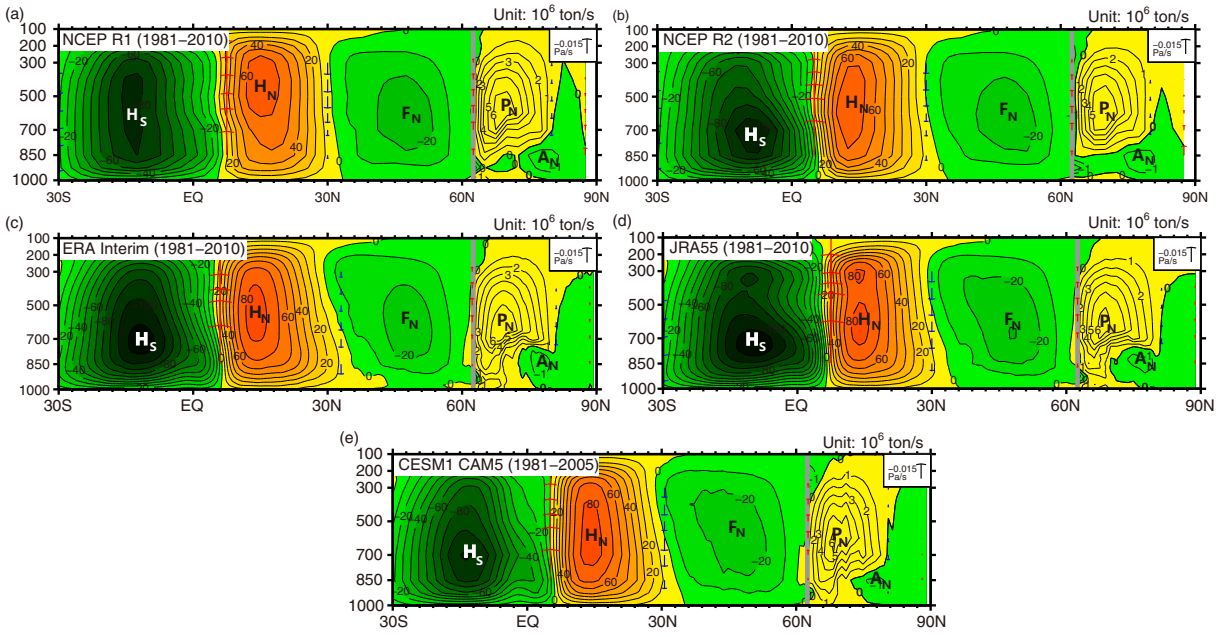

Fig. 5. Same as Fig. 3 except the climatic annual-mean MSFs (106 ton s^{-1}) averaged over 30 yr (1981–2010) were calculated by the four reanalysis products of (a) NCEP R1, (b) NCEP R2, (c) ERA Interim, (d) JRA55 and (e) the ensemble mean data of three CESM1 CAM5 historical runs over 25 yr (1981–2005), respectively. Red and blue arrows indicate ascending and descending pressure velocities (-0.015 Pa s^{-1}), respectively.

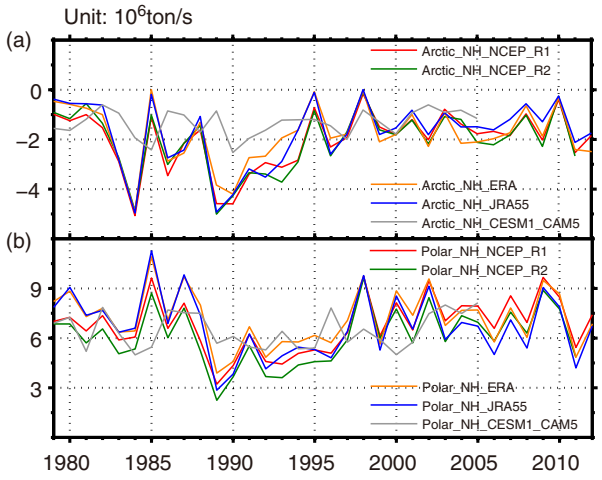

Fig. 6. Annual-mean central MSF intensity series of Polar and Arctic cells from 1979 to 2012. The intensity (10^6 ton s^{-1}) series of (a) the Polar cell and (b) the Arctic cell were calculated with annual-mean MSF from the four reanalysis products (NCEP R1, NCEP R2, ERA Interim, and JRA55) and the ensemble mean of three historical runs (CESM1 CAM5).

and additional evidence will be given in this section to support the existence of the Arctic cell. It is noted that in Fig. 2 the Hadley, Ferrel and Polar cells have complex structures. They may split, shift and merge in a complicated manner over time. Near the surface, topographic, frictional and diabatic processes also affect these circulations.

The number of meridional cells existing in the NH troposphere can be calculated using eq. (3) and illustrated by MSFs. Figures 3 and 5 show the total distribution of the MSFs. It is well known that the tropical Hadley cell is dynamically and thermally driven by the zonally averaged turbulent drag force $[\tilde{X}]$ and diabatic heating rate $[\tilde{J}]$ while the Ferrel cell is believed that the zonally averaged stationary eddy heat flux $[\tilde{v}^*\tilde{T}^*]$ and eddy momentum flux $[\tilde{u}^*\tilde{v}^*]$ make dominant contributions (Holton, 2004). Figure 7 shows the northward eddy heat flux $[\tilde{v}^*\tilde{T}^*]$ in the NH calculated from the ERA reanalysis in October, November, December, and January. As expected, positive and strong centres of the eddy heat flux exist in the middle latitudes (30°N–60°N) while weak and negative centres are found in the tropics. From the negative weak centre (H) to

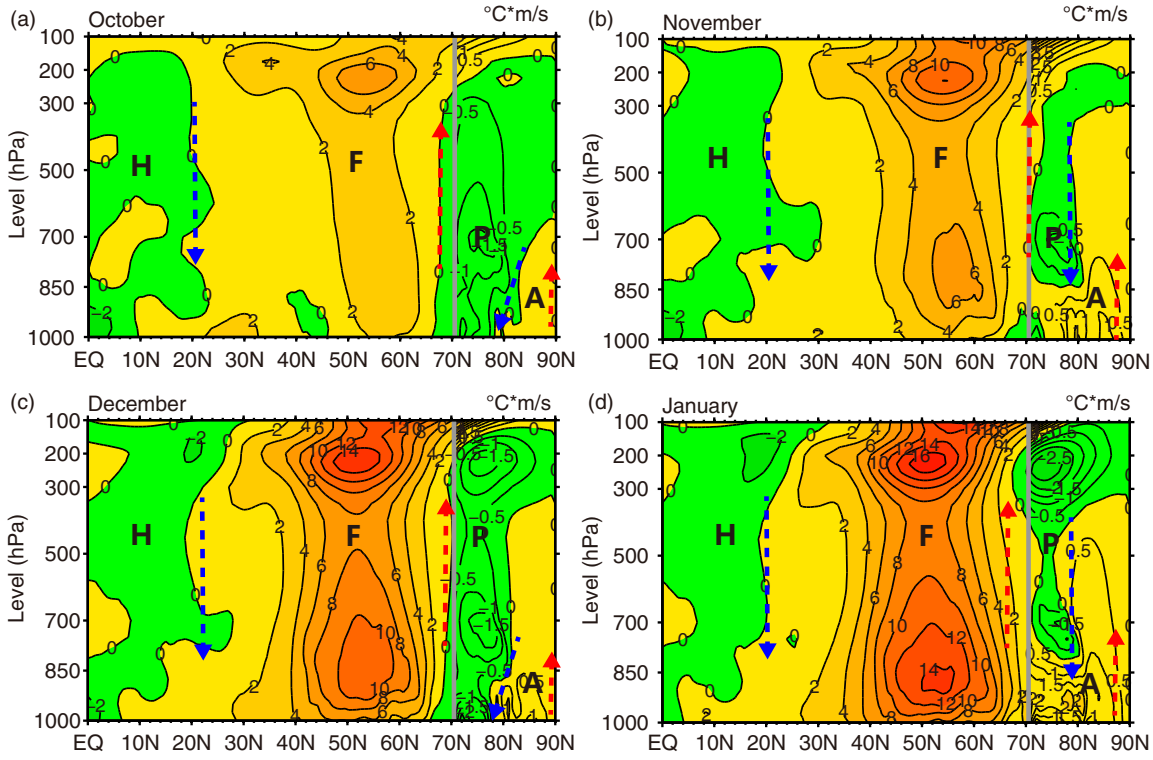

Fig. 7. Northward eddy heat flux ($[\tilde{v}^*\tilde{T}^*]$, yellow-red shading for positive and green for negative, 2°C m s^{-1} interval in mid-low latitudes and 0.5°C m s^{-1} interval in the Arctic) calculated from a 30-yr (1981–2010) average of ERA Interim reanalysis product in the Northern Hemisphere in (a) October, (b) November, (c) December, and (d) January. Letters H, F, P and A are central locations of the Hadley, Ferrel, Polar and Arctic cells, respectively. From 'H' to 'F' $-\frac{\partial[\tilde{v}^*\tilde{T}^*]}{\partial y}<0$, i.e. $[\tilde{w}]_i<0$, so there is a descending branch flow (blue dashed arrow) between them while from 'F' to 'P' there is an ascending branch flow (red dashed arrow).

the positive strong centre (F), $-\frac{\partial[\tilde{v}^*\tilde{T}^*]}{\partial y}<0$, i.e. $[\tilde{w}]_i<0$, so there is a descending branch flow (blue dashed arrow) between them. From the positive strong centre (F) to the location of a negative weak centre (P) there is an ascending branch flow (red dashed arrow) because $-\frac{\partial[\tilde{v}^*\tilde{T}^*]}{\partial y}>0$, i.e. $[\tilde{w}]_i>0$. Thus, if the Hadley cell forms in the tropics, the reversed and closed loop next to the Hadley cell should be the Ferrel cell in the middle latitudes. In comparison between Figs. 7 and 3d, it can be identified that the Ferrel cell is mainly contributed by the stationary eddy heat flux. This feature has also been illustrated by Schubert et al. (1990).

In previous studies, no detailed comparison between the high and mid-low latitude stationary eddy heat fluxes was done. As shown by Fig. 7, there are two pairs of negative and positive centres of eddy heat flux, respectively, in mid-low latitudes and high latitudes. The first pair of negative and positive centres of eddy heat flux is indicated by 'H' and 'F' while the second pair is denoted by 'P' and 'A', although the latter are weaker and smaller than that of the former. In Fig. 7, these four centres of eddy flux are near the centres of Hadley, Ferrel, Polar and Arctic cells. Similarly, Fig. 8 shows the northward stationary eddy momentum flux $[\tilde{v}^*\tilde{u}^*]$ in October, November, December, and January in the NH. From an ascending flow (red dashed arrow) to a descending flow (blue dashed arrow), $\frac{\partial[\widetilde{u^*v^*}]}{\partial y}>0$, i.e. $[\tilde{v}]_i>0$, so there is a southerly wind component (white dashed arrow), otherwise a northerly wind component. There are also two pairs of cells described by the eddy momentum flux, respectively, in mid-low and high latitudes. The first pair indicated by 'H' and 'F' is, respectively, near the centres of the Hadley cell and the Ferrel cell, while the second pair denoted by 'P' and 'A' is near the centres of the Polar cell and the Arctic cell. The similar distributions as shown in Figs. 7 and 8 can also be observed from the other three reanalysis products and the model simulation.

The existence of the Arctic cell may also be demonstrated by Fig. 9. In the Arctic, high precipitation rate is mainly concentrated in summer from pentads 29 to 45. During this period, the precipitation rate is more than 1 mm d^{-1} in the Arctic, while in the sub-polar there is a dry zone with the precipitation rate less than 1 mm d^{-1} (Fig. 9a). In the Arctic, there is a year-round low centre of climatic geopotential height at 850 hPa, whereas there is a high zone in the sub-polar region (Fig. 9b). The low centre in

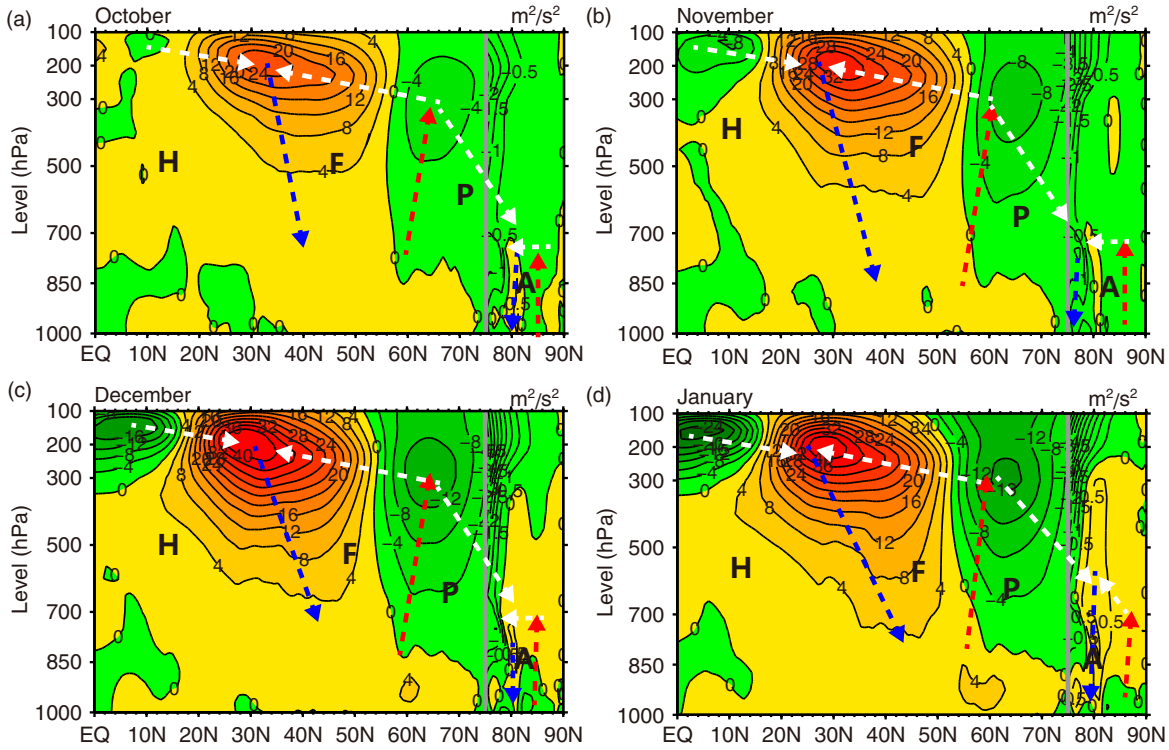

Fig. 8. Same as in Fig. 7 except of the northward eddy momentum flux ($[\tilde{v}^*\tilde{u}^*]$ (yellow-red shading for positive and green for negative, 4 m^2s^{-2} interval in mid-low latitudes and 0.5 m^2s^{-2} interval in the Arctic) calculated from a 30-yr (1981–2010) average of ERA Interim reanalysis in the Northern Hemisphere in (a) October, (b) November, (c) December, and (d) January. From an ascending flow (red dashed arrow) to a descending flow (blue dashed arrow), $\frac{\partial[\tilde{v}^*\tilde{u}^*]}{\partial y}>0$, i.e. $[\tilde{v}]_i>0$, so there is a southerly wind component (white dashed arrow) otherwise a northerly wind component.

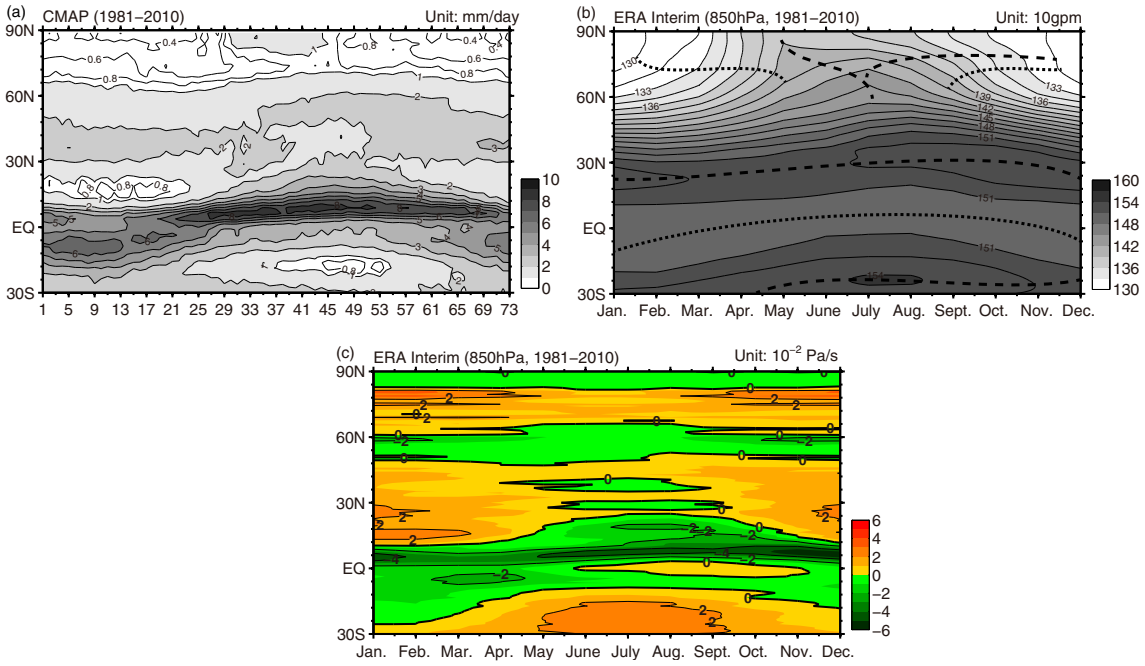

Fig. 9. Meridional (30°S–90°N) and time sections of (a) climatic pentad (1–73) precipitation (grey shading, 1 mm d^{-1} interval) using the enhanced CMAP dataset, (b) monthly-mean geopotential height (grey shading, 30 gpm interval) and (c) vertical pressure velocity (yellow-red for positive and green for negative, 1×10^{-2} Pa s^{-1} interval) at 850 hPa using the ERA-Interim reanalysis product averaged over 30-yr (1981–2010). Low precipitation rate (<1 mm d^{-1}) along the sub-polar zone separates two high precipitation (>1 mm d^{-1}) zones, respectively, in the Arctic and middle latitudes (a). Three height ridges (dashed line) separate a low-pressure centre in the Arctic and two height troughs (dotted line), respectively, in the equator and middle latitudes (b). Two major descending flow zones (red shading) in the sub-polar and the sub-tropical regions separate three ascending flow zones (green shading) in the Arctic, middle latitudes and tropical regions, respectively (c).

geopotential height and the high precipitation rate in the Arctic are closely linked to an ascending flow region at 850 hPa (Fig. 9c). In the traditional three-cell model, the Polar cell ranges from 60 to 90°N. In that case, the low precipitation rate, the high pressure system and the descending flow are expected to exist climatologically in the Arctic, which is inconsistent with our results. Fig. 9 adds a set of additional evidences to challenge the traditional three-cell model.

5. Impact of the Arctic cell on Arctic sea ice

If the Arctic cell is real and climatologically active in the high latitudes, it should have a significant impact on Arctic climate change. The Arctic sea ice cover has undergone a substantial long-term decline with superimposed interannual SIM events over the last decades. The existence of the Arctic cell can also be evaluated from its effect on sea ice change in the high latitudes. The formation of new sea ice is followed by a strong cold air outbreak, when a cold air mass with a lower temperature (below 0°C) than SST passes by. The cold air outbreak is a consequence of strong descending flow in high latitudes and northerly-wind temperature advection near the surface, which are dependent upon the seasonal migration of the Polar and Arctic cells. The adiabatic warming during the descending process is weaker than the cooling of the vertical and horizontal clod advections, which can be observed from the following analysis.

Figure 10 shows the intensities of the descending and ascending flow branches in the NH high latitudes. The descending flow zone is concentrated from 69 to 82°N while the ascending flow zone is located beyond 83°N. The strongest descending flow is climatologically observed in the boreal winter (Fig. 10d). From Fig. 10, we can define two areas with the DFI averaged over 500–850 hPa from 75 to 83°N and the ascending flow intensity (AFI) averaged over 500–850 hPa from 85 to 90°N based on the ERA and JRA55 reanalysis products.

Figure 11a and b show the climatic DFI and AFI. The DFI derived from the two reanalysis products is consistent, with the maximal DFI in February and the minimal DFI in July (Fig. 11a), while the negative AFI peaks in January and July (Fig. 11b). The total SIE and mean SIC, which indicate the amount of sea ice in the NH, reaches maximum in March and minimum in September (Serreze et al., 2007;

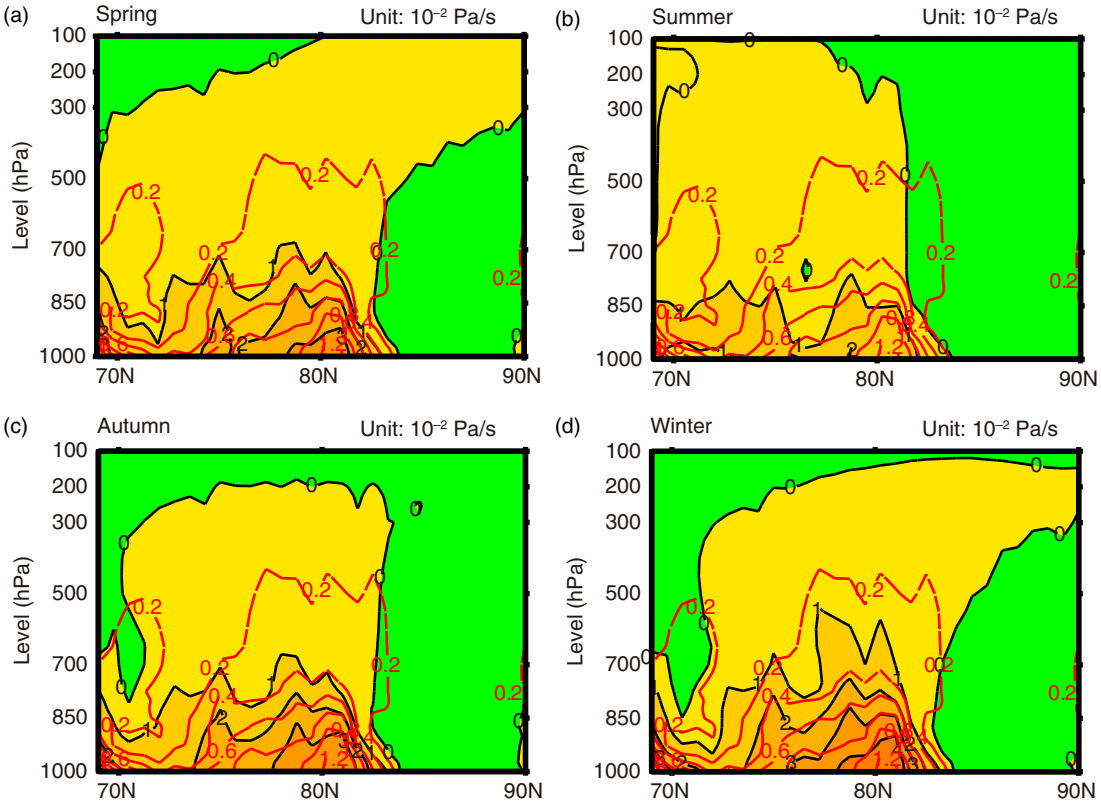

Fig. 10. Climatic seasonal-mean vertical velocity. Vertical and meridional sections of zonally averaged descending (yellow) and ascending (green) pressure velocities (solid line, 1×10^{-2} Pa s^{-1} interval) and standard deviation (red dashed line, 0.2×10^{-2} Pa s^{-1} interval) between 69 and 90°N and from 100 to 1000 hPa in the boreal (a) spring, (b) summer, (c) autumn and (d) winter using a 30-yr average (1981–2010) of the ERA-Interim reanalysis product.

Budikova, 2009) (Fig. 11c). In summer and autumn, the minimal SIE and SIC lag the minimal DFI and the maximal AFI by about 2 months. This lag relationship implies that the weakening DFI and the strengthening AFI in July would reduce cold air transport vertically and horizontally from 80 to 70°N, resulting in the minimal SIE or SIC usually happening between 80 and 70°N in late autumn (Figs. 10 and 12). It is also noted that the climatic temperature is always low in the higher latitudes and aloft but varies with season (Fig. 12). In winter the strongest descending flow ($>4 \times 10^{-2}$ Pa s^{-1}) is climatologically located in the lower troposphere near the 80°N (Fig. 10d) while there is a layer of temperature inversion below 925 hPa due to the effects of radiation and temperature advection in the high latitudes (Fig. 12d).

The climatic DFI is about two times stronger than the AFI, which motivates us to focus on exploring the relationship between the DFI and the SIC. After removing the climatic seasonal cycle and long-term linear trends of SIE (-0.272×10^6 km^2 per decade), SIC (-1.33% per decade) and the DFI (0.012×10^{-2} Pa s^{-1} per decade), the 15-month running means of the three indices are calculated. A significant correlation ($r = 0.79$) is detected between SIC and SIE. A lagged correlation analysis shows that the DFI anomaly statistically leads the SIC anomaly by about 10 months with a maximal positive correlation coefficient of 0.54, reaching the 99% confidence level using a Student's *t*-test. This implies the Polar–Arctic cell interaction is a strong factor inducing large-scale sea-ice change (Fig. 13a). This significant correlation provides a potential for operational seasonal sea ice forecasts. Fig. 13a displays a total of 12 positive-negative DFI peaks and a total of 8 positive-negative SIC peaks exceeding two thresholds (dashed lines, $\pm 0.1 \times 10^{-2}$ Pa/s or $\pm 1\%$) since 1980. The DFI contains a clear precursory signal of SIC. In fact, most of the SIC peaks, i.e. 66.7% (8/12), were associated with prior peaks of the DFI, indicating that the DFI is a useful early signal for seasonal prediction of SIC.

When a negative SIC anomaly less than -1% persists for at least half a year, it is regarded as a warm Arctic event. Similarly, a cold Arctic event is defined here as SIC anomaly greater than $+1\%$ that persists for at least half a year. Among the five warm events indicated in Fig. 13a, two recorded September SIM events in 2007

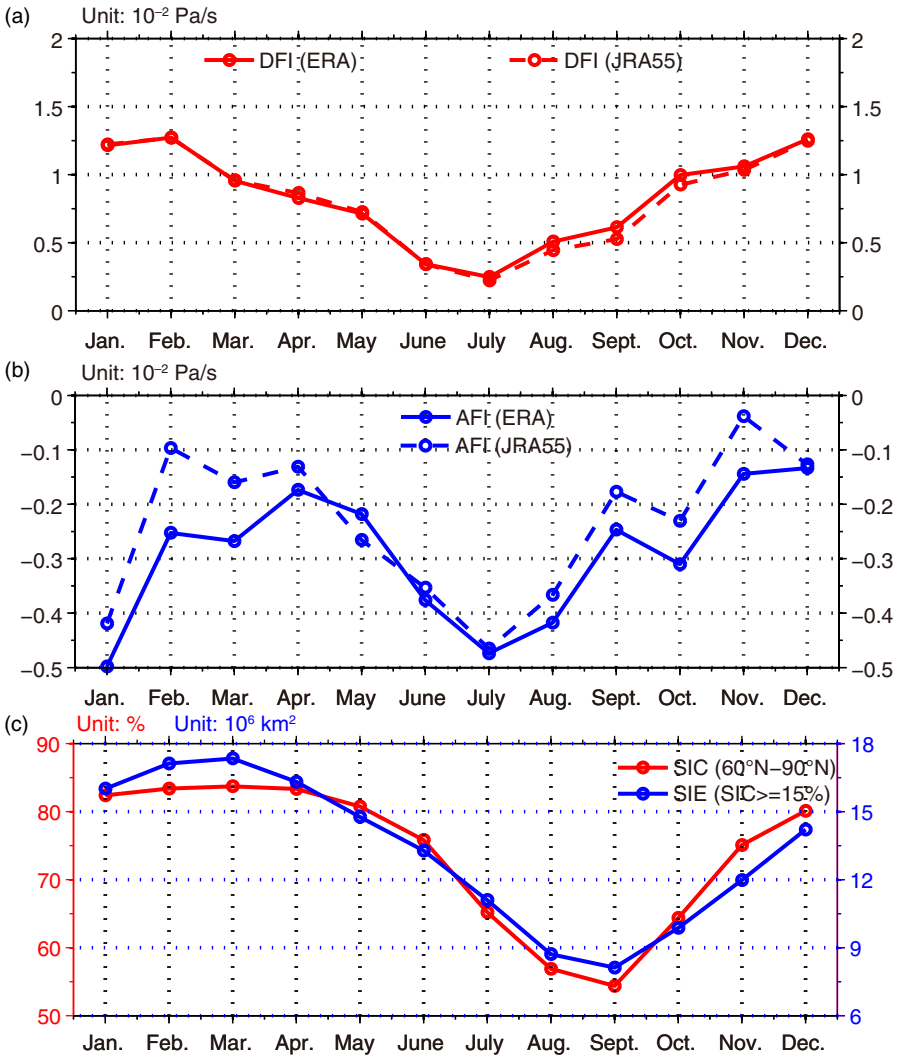

Fig. 11. Seasonal series of (a) the monthly-mean descending flow intensity (DFI) (10^{-2} Pa s^{-1}) averaged over 500–850 hPa from 75 to 83°N based on ERA and JRA55 reanalysis products, (b) the monthly-mean ascending intensity (AFI) averaged over 500–850 hPa from 85 to 90°N, and (c) sea ice concentration (SIC,%) and sea ice extent (SIE, the area of sea ice with SIC > 15%,10^6 km^2) averaged over the latitude band of 60–90°N based on the HadISST dataset.

(e.g. Kay et al., 2008; L'Heureux et al., 2008; Graversen et al., 2011) and 2012 (e.g. Bennartz et al., 2013; Parkinson and Comiso, 2013) were particularly studied. The strongest warm event with the SIC anomaly $< -2\%$ persisting for 15 months was centred in September 2007 and the last warm event with the SIC anomaly $< -1.5\%$ was centred in September 2012. Similarly, the most recent four SIM events have their negative SIC anomaly peaked or centred in September.

Previous studies only focused on the last two Arctic SIM events mentioned above. Here we give a composite result of the five warm or SIM events occurring in the last three decades. The central month of warm events is easily determined at its negative SIC peak or the middle month of each period with SIC less than -1%. For each of the five warm events, its early signal can be found from corresponding persistent negative DFI anomalies (Fig. 13a). Five central months and their 15 consecutive months of DFI anomaly episodes are also determined from the series of DFI anomalies using the same method (negative DFI peak or the middle month of each period with DFI less than -0.1×10^{-2} Pa/s). The five DFI anomaly episodes lead the five Arctic warm events by about 14 months on average. The composite averages of five negative SIC and DFI anomaly events are shown in Fig. 13b and d, respectively.

Three major cold events are also identified in Fig. 13a when using SIC anomaly $> +1\%$ as a threshold. A signal

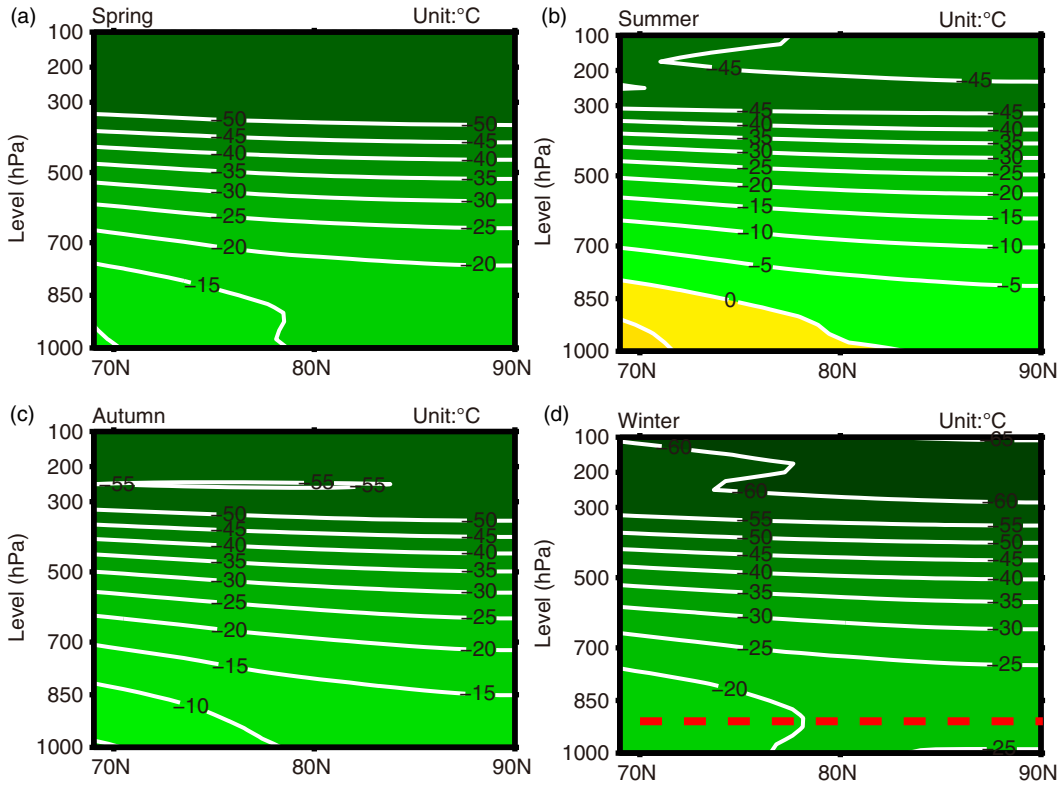

Fig. 12. Vertical and meridional sections of zonally averaged climatic seasonal-mean temperature (5°C interval) between 69 and 90°N and from 100 to 1000 hPa in the boreal (a) spring, (b) summer, (c) autumn and (d) winter using a 30-yr average (1981–2010) of the ERA-Interim reanalysis product. In (d), below the red dashed line (925 hPa) is the temperature inversion layer.

of positive DFI anomalies can be found before the cold event '**A**' while another positive DFI anomaly was strong and simultaneously coincided with the cold event '**B**'. The composite averages of the three positive SIC and DFI anomalies are shown in Fig. 13c and e, respectively. The two composites of SIC anomalies show a significant contrast, particularly in the Eastern Hemisphere (Fig. 13b vs. 13c). Other significant contrasts are from the composites of DFI anomalies illustrated in Fig. 13d and e as well as those showing horizontal temperature advections in Fig. 13f and g. In the mid-low troposphere between 78 and 85°N, a negative DFI anomaly (Fig. 13d) is associated with an Arctic warm (negative SIC anomaly) pattern (Fig. 13b), while a positive DFI anomaly (Fig. 13e) is linked with an Arctic cold (positive SIC anomaly) pattern (Fig. 13c). The cold (Fig. 13f) and warm (Fig. 13g) horizontal advections below 850 hPa can well explain the Arctic warm (negative SIC anomaly) (Fig. 13b) and cold (positive SIC anomaly) (Fig. 13c) patterns. This finding strongly supports the notion that the Polar and Arctic cells have a strong impact on the Arctic sea ice variation through the descending flow and the horizontal temperature advection between them at the interannual timescale.

Two interesting interaction mechanisms can be summarised from Figs. 7, 8 and 13. The strengthening meridional eddy heat and momentum fluxes from 70°N to 80°N (Figs. 7 and 8) would intensify the Polar cell and weaken the Arctic cell, causing a positive DFI anomaly (Fig. 13e) and a cold horizontal advection (Fig. 13g). These lead to a positive SIC anomaly (Fig. 13c) in the Arctic. The reverse influence pathway can be observed from a negative DFI (Fig. 13d) and a warm horizontal advection (Fig. 13f), resulting in a negative SIC anomaly (Fig. 13b).

6. Conclusions

This paper confirmed that there is a fourth meridional climatic pattern of atmospheric circulation, named as the Arctic cell, in the NH high latitudes beyond 80°N. More specifically, the following conclusions were drawn.

- **The Arctic cell is confirmed by the current reanalysis products and model simulations.** We, using current widely applied four reanalysis products and one climate model simulation, first confirmed that the Arctic cell is observable in all the five datasets. The existence of the Arctic cell was also indirectly

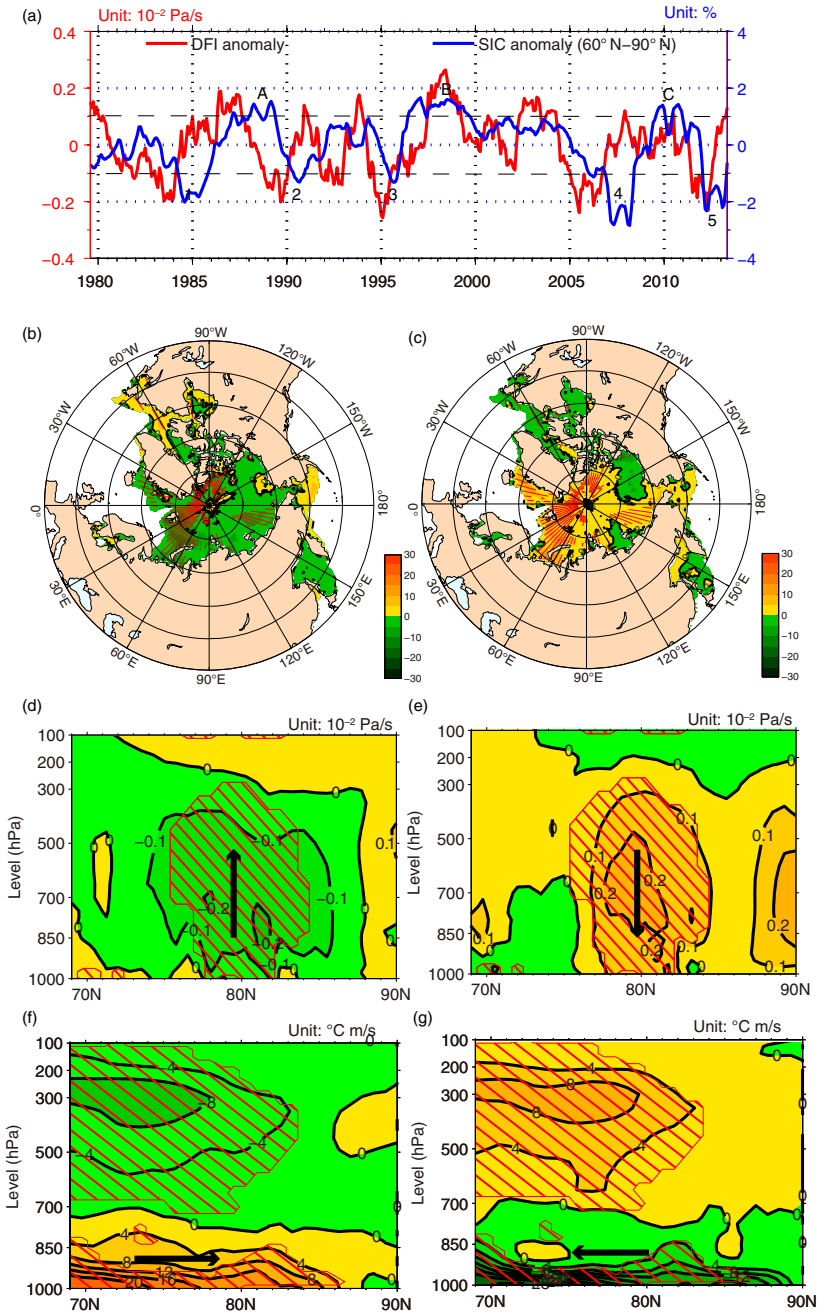

Fig. 13. DFI and SIC anomalies from time series to spatial distributions. (a) Monthly-mean time series of the DFI anomalies (red line, 10^{-2} Pa s^{-1}) and the SIC anomalies (blue line,%) averaged over the latitude band of 60–90°N after removing their linear trends from 1979 to 2013 and calculating the 15-month running mean; (b) Composite average of SIC anomalies (yellow-red shading for positive and green for negative, 5% interval) by five warm cases with 15 consecutive months centred in January 1985, September 1990, September 1995, September 2007, and September 2012; Same as (b) but for (c) three cold cases centred in October 1988, June 1998, and April 2010; (d) Composite average of DFI anomalies (yellow as descending, green as ascending, 0.1×10^{-2} Pa s^{-1} interval) with 15 consecutive months centred in July 1983, June 1989, December 1994, December 2005, and January 2012; Same as (d) but for (e) three descending flow anomalies centred in January 1987, April 1998, and February 2010; (f) same as (d) but for composite average of meridional temperature advection anomaly (yellow as warm advection, green as cold advection, 4°C m s^{-1} interval); (g) same as (f) but for three periods in (e). In (a), the numbers denote five warm events while the capital letters (A, B and C) are three cold events. In (d) and (e), the arrows indicate the anomalous ascending and descending flows, respectively. In (g) and (f), the arrows indicate the anomalous warm and cold advection, respectively. The red-lined area in the last six panels covers the region reaching the 95% confidence level.

confirmed by the climatic pentad precipitation, which records a high precipitation rate near the North Pole with a climatic ascending flow while a low precipitation rate and a climatic descending flow in the sub-polar zone. The Arctic cell exists in all individual monthly-, seasonal- and annual-mean streamlines and MSFs, although their intensities and locations vary.

- **The existence of the Arctic cell is forced by eddy heat and momentum fluxes in high latitudes.** Dynamically, the Arctic cell not only satisfies the conservation of angular momentum, but is also forced by eddy heat and momentum fluxes in high latitudes. The Hadley cell and the Polar cell are two direct meridional circulations driven mainly by the diabatic heating rate and zonally averaged climatic turbulent drag, while the Ferrel cell as an indirect meridional circulation is mainly driven by the zonally averaged stationary eddy heat and eddy momentum fluxes, so does the Arctic cell. The calculated stationary eddy heat and eddy momentum fluxes show that there are two pairs of meridional cells in the NH, the Hadley and Ferrel cells in the mid-low latitudes and the Polar and Arctic cells in the high latitudes.
- **The Arctic cell is one of the main components in the Arctic climate system with atmosphere–ocean–ice (snow) interactions.** We found that the spread of SIE is followed by a breaking cold-air mass with strong descending flow and surface cold advection from 80°N to the sub-polar region. The result shows that the change in Arctic sea ice concentration lags the variations of descending air flow intensity associated with the Polar and Arctic cells by about 2 months in the climatic annual cycle and by about 10 months for the interannual anomaly. Five Arctic SIM events during the last three decades support this finding. Therefore, this work provides a new perspective in understanding the relationship between atmospheric circulation and sea-ice variations, and for predicting the Arctic sea ice changes.

7. Acknowledgements

The authors thank the two anonymous reviewers for their valuable comments and suggestions, and Mr. Jeremy Cheuk-Hin Leung for editing the final manuscript to improve the paper. Weihong Qian thanks Drs. Jun Du, Yi Deng, Minghua Zhang, Guangjun Zhang and Chidong Zhang for their useful suggestions. This work was supported by the Strategic Priority Research Program of the Chinese Academy of Sciences (XDA05090407) and the National Natural Science Foundation of China (41375073). Deliang Chen was supported by the Swedish strategic research areas MERGE and BECC, and Swedish Research Council.

References

Ahrens, C. D. 2012. *Meteorology Today: An Introduction to Weather, Climate, and the Environment*. Cengage Learning, Boston.

Bennartz, R., Shupe, M. D., Turner, D. D., Walden, V. P., Steffen, K. and co-authors. 2013. July 2012 Greenland melt extent enhanced by low-level liquid clouds. *Nature*. **496**(7443), 83–86. DOI: 10.1038/nature12002.

Bromwich, D. H., Fogt, R. L., Hodges, K. I. and Walsh, J. E. 2007. A tropospheric assessment of the ERA-40, NCEP, and JRA-25 global reanalyses in the Polar regions. *J. Geophys. Res.* **112**, D10111. DOI: 10.1029/2006JD007859.

Budikova, D. 2009. Role of Arctic sea ice in global atmospheric circulation: a review. *Glob. Planet. Change* **68**(3), 149–163. DOI: 10.1016/j.gloplacha.2009.04.001.

Chen, G., Iwasaki, T., Qin, H. and Sha, W. 2014b. Evaluation of the warm-season diurnal variability over East Asia in recent reanalyses JRA-55, ERA-Interim, NCEP CFSR, and NASA MERRA. *J. Clim.* **27**(14), 5517–5537. DOI: 10.1175/JCLI-D-14-00005.1.

Chen, S., Wei, K., Chen, W. and Song, L. 2014a. Regional changes in the annual mean Hadley circulation in recent decades. *J. Geophys. Res.* **119**(13), 7815–7832. DOI: 10.1002/2014JD021540.

Cohen, J., Screen, J. A., Furtado, J. C., Barlow, M., Whittleston, D. and co-authors. 2014. Recent Arctic amplification and extreme mid-latitude weather. *Nat. Geosci.* 7(9), 627–637. DOI: 10.1038/NGEo2234.

Compo, G. P., Whitaker, J. S., Sardeshmukh, P. D., Matsui, N., Allan, R. J. and co-authors. 2011. The twentieth century reanalysis project. *Q. J. Roy. Meteorol. Soc.* **137**, 1–28. DOI: 10.1002/qj.776.

Dee, D. P., Uppala, S. M., Simmons, A. J., Berrisford, P., Poli, P. and co-authors. 2011. The ERA-Interim reanalysis: configuration and performance of the data assimilation system. *Q. J. Roy. Meteorol. Soc.* **137**, 553–597. DOI: 10.1002/qj.828.

Deser, C. and Teng, H. 2008a. Recent trends in Arctic sea ice and the evolving role of atmospheric circulation forcing, 1979–2007. In: *Arctic Sea Ice Decline: Observations, Projections, Mechanisms, and Implications* (eds. E. T. Deweaver, C. M. Bitz, and L. B. Tremblay), American Geophysical Union, Washington, pp. 7–26. DOI: 10.1029/180GM03.

Deser, C. and Teng, H. 2008b. Evolution of Arctic sea ice concentration trends and the role of atmospheric circulation forcing, 1979–2007. *Geophys. Res. Lett.* **35**, L02504. DOI: 10.1029/2007GL032023.

Deser, C., Walsh, J. E. and Timlin, M. S. 2000. Arctic sea ice variability in the context of recent atmospheric circulation trends. *J. Clim.* **13**(3), 617–633. DOI: 10.1175/1520-0442(2000)013 < 0617:ASIVIT > 2.0.CO;2.

Devasthale, A., Sedlar, J., Koenigk, T. and Fetzer, E. J. 2013. The thermodynamic state of the Arctic atmosphere observed by AIRS: comparisons during the record minimum sea ice extents

of 2007 and 2012. *Atmos. Chem. Phys.* **13**(15), 7441–7450. DOI: 10.5194/acp-13-7441-2013.

Ding, Q. H., Wallace, J. M., Battisti, D. S., Steig, E. J., Gallant, A. J. E. and co-authors. 2014. Tropical forcing of the recent rapid Arctic warming in northeastern Canada and Greenland. *Nature*. **509**(7499), 209–212. DOI: 10.1038/nature13260.

Ding, T. and Qian, W. H. 2012. Statistical characteristics of heat wave precursors in China and model prediction. *Chin. J. Geophys.* **5**, 1472–1486. DOI: 10.6038/j.issn.0001-5733.2012.05.005 (in Chinese).

Dong, X. Q., Zib, B. J., Xi, B. K., Stanfield, R., Deng, Y. and co-authors. 2014. Critical mechanisms for the formation of extreme arctic sea-ice extent in the summers of 2007 and 1996. *Clim. Dynam.* **43**(1–2), 53–70. DOI: 10.1007/s00382-013-1920-8.

Ebita, A., Kobayashi, S., Ota, Y., Moriya, M., Kumabe, R. and co-authors. 2011. The Japanese 55-year reanalysis "JRA-55": an interim report. *J. Meteorol. Soc. Japan.* **7**, 149–152. DOI: 10.2151/sola.2011-038.

Gon, Z. S., Wang, P. X. and Ma, J. 2002. Application of a simplified calculation scheme for mean meridional circulation mass stream function. *J. Nanjing Inst. Meteorol.* **25**(3), 328–333 (in Chinese).

Graversen, R. G., Mauritsen, T., Tjernstrom, M., Kallen, E. and Graversen, G. 2008. Vertical structure of recent Arctic warming. *Nature*. **451**, 53–56. DOI: 10.1038/nature06502.

Graversen, R. G., Mauritsen, T., Drijfhout, S., Tjernstrom, M. and Martensson, S. 2011. Warm winds from the Pacific caused extensive Arctic sea-ice melt in summer 2007. *Clim. Dynam.* **36**(11–12), 2103–2112. DOI: 10.1007/s00382-010-0809-z.

Hansen, J. and Nazarenko, L. 2004. Soot climate forcing via snow and ice albedo. *Proc. Natl Acad. Sci. USA*. **101**, 423–428. DOI: 10.1073/pnas.2237157100.

Holton, J. R. 2004. *An Introduction to Dynamic Meteorology*. Academic Press, New York.

Honda, M., Inoue, J. and Yamane, S. 2009. Influence of low Arctic sea-ice minima on anomalously cold Eurasian winters. *Geophys. Res. Lett.* **36**, L08707. DOI: 10.1029/2008GL037079.

Hu, A., Rooth, C., Bleck, R. and Deser, C. 2002. NAO influence on sea ice extent in the Eurasian coastal region. *Geophys. Res. Lett.* **29**(22), 2053. DOI: 10.1029/2001GL014293.

Hu, Y. Y. and Fu, Q. 2007. Observed poleward expansion of the Hadley circulation since 1979. *Atmos. Chem. Phys.* **7**, 5229–5236. DOI: 10.5194/acp-7-5229-2007.

Huang, J., Du, J. and Qian, W. H. 2015. A comparison between generalized beta-advection model and classical beta-advection model in predicting and understanding unusual typhoon tracks in eastern China seas. *Weather. Forecast.* **30**, 771–792. DOI: 10.1175/WAF-D-14-00073.1.

Jaiser, R., Dethloff, K., Handorf, D., Rinke, A. and Cohen, J. 2012. Impact of sea ice cover changes on the Northern Hemisphere atmospheric winter circulation. *Tellus A*. **64**, 11595. DOI: 10.3402/tellusa.v64i0.11595.

Jeong, J.-H., Kug, J.-S., Linderholm, H. W., Chen, D., Kim, B.-M. and co-authors. 2014. Intensified Arctic warming under greenhouse warming by vegetation–atmosphere–sea ice interaction. *Environ. Res. Lett.* **9**(9), 094007. DOI: 10.1088/1748-9326/9/9/094007.

Kahl, J. D., Serreze, M. C. and Schnell, R. C. 1991. The historical Arctic rawinsonde archive. In: *Climate Monitoring and Diagnostics Laboratory No.19. Summary report 1990* (eds. E. E. Ferguson and R. M. Rosson), National Oceanic and Atmospheric Administration, Boulder, CO, pp. 95–98.

Kahl, J. D., Serreze, M. C., Shiotani, S., Skony, S. M. and Schnell, R. C. 1992. In situ meteorological sounding archives for Arctic studies. *Bull. Am. Meteorol. Soc.* **73**, 1824–1830. DOI: 10.1175/1520-0477(1992)073<1824:ISMSAF>2.0.CO;2.

Kalnay, E., Kanamitsu, M., Kistler, R., Collins, W., Deaven, D. and co-authors. 1996. The NCEP/NCAR 40-year reanalysis project. *Bull. Am. Meteorol. Soc.* **77**, 437–471. DOI: 10.1175/1520-0477(1996)077<0437:TNYRP>2.0.CO;2.

Kanamitsu, M., Ebisuzaki, W., Woollen, J., Yang, S. K., Hnilo, J. J. and co-authors. 2002. NCEP–DOE AMIP-II reanalysis (R-2). *Bull. Am. Meteorol. Soc.* **83**, 1631–1643. DOI: 10.1175/BAMS-83-11-1631.

Kay, J. E., L'Ecuyer, T., Gettelman, A., Stephens, G. and O'Dell, C. 2008. The contribution of cloud and radiation anomalies to the 2007 Arctic sea ice extent minimum. *Geophys. Res. Lett.* **35**, L08503. DOI: 10.1029/2008GL033451.

Kumar, A., Perlwitz, J., Eischeid, J., Quan, X. W., Xu, T. Y. and co-authors. 2010. Contribution of sea ice loss to Arctic amplification. *Geophys. Res. Lett.* **37**(21), L21701. DOI: 10.1029/2010GL045022.

L'Heureux, M. L., Kumar, A., Bell, G. D., Halpert, M. S. and Higgins, R. W. 2008. Role of the Pacific-North American (PNA) pattern in the 2007 Arctic sea ice decline. *Geophys. Res. Lett.* **35**, L20701. DOI: 10.1029/2008GL035205.

Lindzen, R. S. and Hou, A. Y. 1988. Hadley circulations for zonally averaged heating centred off the equator. *J. Atms. Sci.* **45**(17), 2416–2427. DOI: 10.1175/1520-0469(1988)045<2416:HCFZAH>2.0.CO;2.

Mitas, C. M. and Clement, A. 2005. Has the Hadley cell been strengthening in recent decades? *Geophys. Res. Lett.* **32**(3), L03809. DOI: 10.1029/2004GL021765.

Neale, R., Richter, J. H., Conley, A., Park, S., Lauritzen, P. H. and co-authors. 2010. *Description of the NCAR Community Atmosphere Model (CAM5.0)*. NCAR/TN-486+STR, NCAR Tech. Rep., Boulder, CO, 268 pp.

Onogi, K., Tslttsui, J., Koide, H., Sakamoto, M., Kobayashi, S. and co-authors. 2007. The JRA-25 reanalysis. *J. Meteorol. Soc. Jpn.* **85**(3), 369–432. DOI: 10.2151/jmsj.85.369.

Parkinson, C. L. and Comiso, J. C. 2013. On the 2012 record low Arctic sea ice cover: combined impact of preconditioning and an August storm. *Geophys. Res. Lett.* **40**(7), 1356–61. DOI: 10.1002/grl.50349.

Persson, A. 2006. Hadley's principle: understanding and misunderstanding the trade winds. *Hist. Meteorol.* **3**, 17–42.

Prinsenberg, S. J., Peterson, I. K., Narayanan, S. and Umoh, J. U. 1997. Interaction between atmosphere, ice cover, and ocean off Labrador and Newfoundland from 1962–1992. *Can. J. Aquat. Sci.* **54**(S1), 30–39. DOI: 10.1139/f96-150.

Qian, W. H., Chen, Y., Jiang, M. and Hu, Q. 2015b. An anomaly-based method for identifying signals of spring and autumn low temperature events in the Yangtze River Valley, China. *J. Appl. Meteorol. Clim.* **54**, 1216–1233.

Qian, W. H. and Jiang, M. 2014. Early signals of synoptic-scale atmospheric anomalies associated with the summer low temperature events in Northeast China. *Meteorol. Atmos. Phys.* **124**(1–2), 33–46. DOI: 10.1007/s00703-013-0306-0.

Qian, W. H., Shan, X. L., Liang, H. Y., Huang, J. and Leung, C. H. 2014. A generalized beta advection model to improve unusual typhoon track prediction by decomposing total flow into climatic and anomalous flows. *J. Geophys. Res.* **119**(3), 1097–1117. DOI: 10.1002/2013JD020902.

Qian, W. H., Wu, K. J. and Liang, H. Y. 2015a. Arctic and Antarctic cells in the troposphere. *Theor. Appl. Climatol.* DOI: 10.1007/s00704-015-1485-z.

Rayner, N. A., Parker, D. E., Horton, E. B., Folland, C. K., Alexander, L. V. and co-authors. 2003. Global analyses of sea surface temperature, sea ice, and night marine air temperature since the late nineteenth century. *J. Geophys. Res.* **108**(D14), 1–29. DOI: 10.1029/2002JD002670.

Rienecker, M. M., Suarez, M. J., Gelaro, R., Todling, R., Bacmeister, J. and co-authors. 2011. MERRA: NASA's modern-era retrospective analysis for research and applications. *J. Clim.* **24**, 3624–3648. DOI: 10.1175/JCLI-D-11-00015.1.

Rigor, I. G., Wallace, J. M. and Colony, R. L. 2002. Response of sea ice to the Arctic oscillation. *J. Clim.* **15**, 2648–2663. DOI: 10.1175/1520-0442(2002)015 < 2648:ROSITT > 2.0.CO;2.

Saha, S., Moorthi, S., Pan, H.-L., Wu, X. R., Wang, J. D. and co-authors. 2010. The NCEP climate forecast system reanalysis. *Bull. Am. Meteorol. Soc.* **91**(8), 1015–1057. DOI: 10.1175/2010BAMS3001.1.

Sato, K., Inoue, J. and Watanabe, M. 2014. Influence of the Gulf Stream on the Barents Sea ice retreat and Eurasian coldness during early winter. *Environ. Res. Lett.* **9**, 084009. DOI: 10.1088/1748-9326/9/8/084009.

Schubert, S., Park, C. K., Higgins, W., Moorthi, S. and Suarez, M. 1990. *An Atlas of ECMWF Analyses (1980–1987) Part 1: First Moment Quantities*. NOAA Technical Memorandum 100747, NASA/GSFC Tech. Mem. 100747, Greenbelt, Maryland.

Screen, J. A. and Simmonds, I. 2010. The central role of diminishing sea ice in recent Arctic temperature amplification. *Nature*. **464**(7293), 1334–1337. DOI: 10.1038/nature09051.

Serreze, M. C. and Francis, J. A. 2006. The Arctic amplification debate. *Clim. Change*. **76**, 241–264. DOI: 10.1007/s10584-005-9017-y.

Serreze, M. C., Holland, M. M. and Stroeve, J. 2007. Perspectives on the Arctic's shrinking sea-ice cover. *Science*. **315**, 1533–1536. DOI: 10.1126/science.1139426.

Shindell, D. and Faluvegi, G. 2009. Climate response to regional radiative forcing during the twentieth century. *Nature Geosci.* **2**, 294–300. DOI: 10.1038/ngeo473.

Stachnik, J. P. and Schumacher, C. 2011. A comparison of the Hadley circulation in modern reanalyses. *J. Geophys. Res.* **116**, D22. DOI: 10.1029/2011jd016677.

Taylor, K. E., Stouffer, R. J. and Meehl, G. A. 2012. An overview of CMIP5 and the experiment design. *Bull. Am. Meteorol. Soc.* **93**, 485–498. DOI: 10.1175/BAMS-D-11-00094.1.

Ukita, J., Honda, M., Nakamura, H., Tachibana, Y., Cavalieri, D. J. and co-authors. 2007. Northern Hemisphere sea ice variability: lag structure and its implications. *Tellus A*. **59**(2), 261–272. DOI: 10.111/j.1600-0870.2006.00223.x.

Vihma, T. 2014. Effects of Arctic sea ice decline on weather and climate: a review. *Surv. Geophys.* **35**, 1175–1214. DOI: 10.1007/s10712-014-9284-0.

Wang, P. X. 1994. Diagnosis of mean meridional circulation of the model atmosphere in the GCM with low resolution vertically. *J. Nanjing Inst. Meteorol.* **17**(2), 200–204 (in Chinese).

Xie, P. and Arkin, P. A. 1997. Global precipitation: a 17-year monthly analysis based on gauge observations, satellite estimates, and numerical model outputs. *Bull. Am. Meteorol. Soc.* **78**, 2539–2558. DOI: 10.1175/1520-0477(1997)078 < 2539:GPAYMA > 2.0.CO;2.